Transport properties around the metal-insulator transition for $SrVO_3$ ultrathin films fabricated by electrochemical etching

Hikaru Okuma,* Yumiko Katayama, Keisuke Otomo, and Kazunori Ueno
Department of Basic Science, University of Tokyo, Meguro, Tokyo 153-8902, Japan

(Received 25 May 2021; revised 2 December 2021; accepted 11 January 2022; published 26 January 2022)

By using electrochemical etching, we fabricated conductive ultrathin $SrVO_3$ (SVO) films that exhibited metallic behavior down to 3 monolayers (ML). From an observed systematic change in transport properties with decreasing film thickness, it was found that the disorder in the films remained nearly unchanged during etching, and only the thickness was reduced. This is in contrast to the insulating behavior found for as-deposited SVO ultrathin films. For the etched films, the electron mobility at 200 K decreased with decreasing film thickness below 10 ML, originating from an increased scattering rate and electron effective mass near the metal-insulator transition. A slight upturn in the resistivity and a positive magnetoresistance at low temperatures were typically observed for the etched films down to 3 ML, which was explained by weak antilocalization of electrons in a weakly disordered metal.

DOI: 10.1103/PhysRevB.105.045138

I. INTRODUCTION

A strongly correlated electron system shows a Mott transition due to competition between on-site Coulomb repulsion (U) and a one-electron bandwidth (W) [1,2]. The system becomes a Mott insulator when U/W exceeds a critical value. In addition, strongly correlated metals in the vicinity of an insulator undergo not only a Mott transition but also Anderson localization due to crystal disorder [3]. Therefore, it is difficult to determine whether electron-electron interactions or disorder is the dominant driving force behind the metal-insulator transition (MIT).

$SrVO_3$ (SVO) ($a = 0.3843$ nm) has a $3d^1$ electronic configuration for vanadium and is, thus, a good candidate for studying the MIT in the metallic regime. The control parameters for the Mott transition are bandwidth and band filling [4]. In earlier studies, the MIT was mainly tuned by chemical substitution. For example, the band filling controlled MIT in the $La_{1-x}Sr_xVO_3$ system is induced by an aliovalent A-site substitution [5–7]. On the other hand, the bandwidth change in the $Ca_{1-x}Sr_xVO_3$ (CSVO) system has been studied by isovalent A-site substitution with different ionic radii [8–11]. Taking into account W, $CaVO_3$ (CVO) is expected to be the most insulating. However, CSVO with $x = 0.2$–0.5 is closest to the insulator in the whole composition range [10,11]. This indicates that the dominant driving force for the insulating state is the disorder induced by the solid solution between CVO and SVO. Then, it is necessary to study the electron-electron interaction effect on the MIT to change W with fixed disorder.

In recent years, major improvements in molecular beam epitaxy in oxides have provided high-quality ultrathin films for exhibiting novel physical phenomena that uniquely emerge at heterointerfaces [12,13]. Furthermore, precise thickness control makes it possible to control W by reducing the electronic dimensionality from three dimensions (3D) to two dimensions (2D). Then, we can isolate a change in W from other competitive effects induced by chemical substitution [14–24]. However, studies using a few nanometer thick films showed that the critical thicknesses for the MIT differed by the degree of disorder, such as tensile strain at an interface [14] and surface degradation [19]. In addition, an abrupt increase in resistivity (ρ) at low temperature has also been reported around the critical thicknesses due to disorder, such as oxygen deficiency [15], surface scattering [22], and lattice strain near the magnetic transition [18]. Therefore, such disorder must be controlled for studying the MIT with a change in W in ultrathin films.

For SVO thin films, *in situ* photoemission (PES) showed that Mott insulating states are induced with a thickness of 2–3 monolayers (ML) [25]. Transport studies also showed insulating behavior with an abrupt increase in resistivity in SVO films. However, the critical thickness for the insulator varies between 3 and 8 ML, all of which are thicker than 2 ML [17,20,23,24]. This suggests that the disorder-induced Anderson transition occurs at different thicknesses because each film has different disorder.

In this study, we eliminated differences in disorder between samples by using the electrochemical etching method [26–29]. Disorder in a thin film sample remained unchanged during electrochemical etching, but the dimensionality was changed by a reduction in the film thickness. In addition, the specific adsorptions of anions during electrochemical etching exclude the surface reconstruction and an absorption of air molecules under *ex situ* conditions, which strongly affect the critical thickness of SVO. We applied an electric double layer transistor (EDLT) configuration to SVO films [28,29]. After fixing the disorder, electronic transport properties as a function of the film thickness near the MIT were examined. The etched SVO films with a thickness of 3 ML exhibited conductive behavior, whereas the as-deposited films became

*hikaruokuma613@g.ecc.u-tokyo.ac.jp

 ©2022 American Physical Society

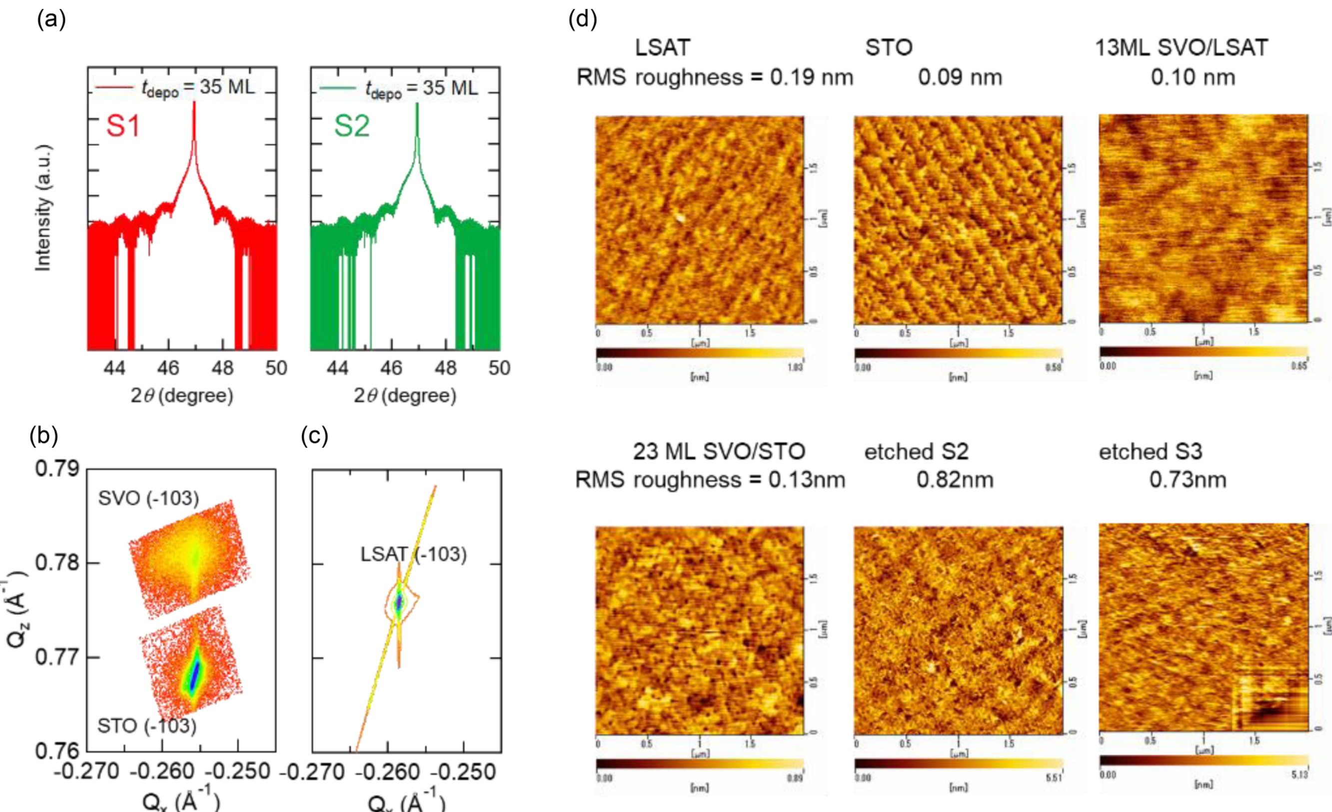

FIG. 1. (a) Out of plane $2\theta/\omega$ scan of as-deposited S1 and S2 films before etching. (b), (c) The reciprocal space mapping on (–103) reflection of as-deposited (b) SVO/STO and (c) SVO/LSAT. (d) AFM surface morphologies of LSAT, STO, 13 ML SVO/LSAT, and 23 ML SVO/STO, electrochemically etched S2 and S3 films, whose root mean square (RMS) roughnesses are 0.19, 0.09, 0.10, 0.13, 0.82, and 0.73 nm, respectively.

good insulators. Then, we elucidated the transport properties of the ultrathin conductive films in the vicinity of the Mott insulator states by measuring the temperature dependence of ρ and magnetoresistance (MR) at low temperature.

II. EXPERIMENT

SVO thin films were deposited on (100)-oriented $(LaAlO_3)_{0.3}(Sr_2AlTaO_6)_{0.7}$ (LSAT) ($a = 0.3868$ nm) and $SrTiO_3$ (STO) ($a = 0.3905$ nm) substrates by the pulsed laser deposition (PLD) method at 10^{-7} Torr and 900 °C. A ceramic target composed of SVO was ablated by a KrF excimer laser ($\lambda = 248$ nm) with a repetition rate of 5 Hz and an energy fluence of 0.97–1.06 J/cm^2. The growth of SVO (100) thin films was confirmed by an out of plane $2\theta/\omega$ scan with x-ray diffraction and XRD (Rigaku, SmartLab), as shown in Fig. 1(a). The smooth interface and epitaxial growth were confirmed with x-ray Laue oscillations and reciprocal space mapping, as shown in Figs. 1(a), and 1(b) and 1(c), respectively. The thicknesses of the films were determined by the deposition rate and confirmed with x-ray Laue oscillations. In addition, the surface uniformity and film thickness were estimated with an atomic force microscope (AFM) and cross-section transmission electron microscopy (TEM), respectively. The AFM surface images and TEM images are shown in Fig. 1(d) and the Supplemental Material, Sec. B [30], respectively.

We fabricated EDLTs on as-deposited films (S1–S3) with a thickness of 35 ML on LSAT. The SVO films were patterned into Hall bars with Au/Ti electrodes, and a Pt wire was placed over the channel and used as a gate electrode. The channel and Pt gate electrodes were covered with an ionic liquid (IL) droplet, *N*, *N*-diethyl-*N*-methyl-*N*-(2-methoxyethyl)ammonium bis (trifluorometh anesulfonyl)imide (DEME-TFSI). The SVO thin films were repeatedly etched at 230 K with a gate bias ranging between –3 and –4.5 V, and the transport properties for the respective thicknesses (t_{etch}) were obtained. We also obtained transport properties for the as-deposited films with various thicknesses (t_{depo}). The transport properties were examined by using the four-probe method and a Hall measurement in a physical properties measurement system (Quantum Design, PPMS) from 2 to 300 K and –3 to 3 T.

A reference EDLT on the as-deposited film on STO (S4) was also made to estimate the thickness of the etched film by an x-ray measurement. Detailed information can be found in the Supplemental Material, Sec. C [30].

III. RESULTS AND DISCUSSION

A. Characterization and etching process of $SrVO_3$ films

Figure 1(a) shows an out of plane $2\theta/\omega$ scan of as-deposited S1 and S2 films on LSAT substrates. For both films, Laue oscillations are clearly observed, indicating a smooth interface between the substrate and the film. Figures 1(b) and 1(c) display the reciprocal space mapping (RSM) on a

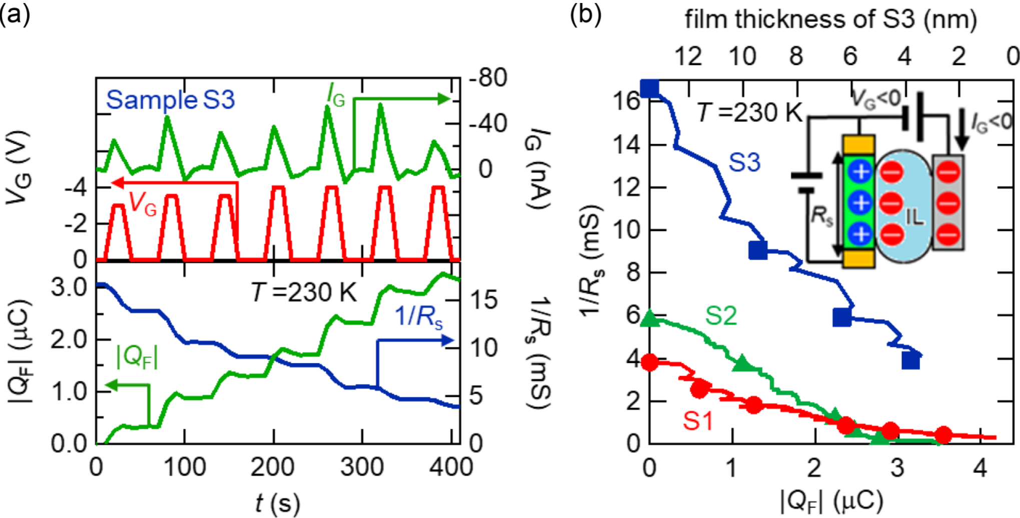

FIG. 2. (a) Time evolution of the gate bias (V_G), gate current (I_G), absolute value of the Faradaic charge ($|Q_F|$), and sheet conductance ($1/R_s$) during electrochemical etching at 230 K for sample S3. (b) $1/R_s$ versus $|Q_F|$ curves for electrochemical etching processes at 230 K for three samples (S1–S3). The inset shows a schematic for an EDLT on an SVO film. I_G flows to a gate electrode by applying V_G, and the anions in the ionic liquid (IL) move to the surface of the SVO film. The surface is etched by an electrochemical reaction.

(–103) reflection of as-deposited SVO/STO and SVO/LSAT, respectively. As shown in Fig. 1(b), the in-plane lattice constant of SVO extracted from RSM is matched with that of STO, confirming the epitaxial growth of SVO on the STO substrate. In the case of SVO/LSAT, the peak of SVO is completely covered with that of LSAT, as seen in Fig. 1(c). This result indicates that SVO is also epitaxially grown on the LSAT substrate, and both the in-plane and out-of-plane lattice constants of the SVO are identical to those of the LSAT substrate. Figure 1(d) displays surface images of LSAT (under ambient conditions after heating treatment at 900 °C in a PLD chamber) and STO substrates, as-deposited 13 ML SVO on LSAT (SVO/LSAT) and 23 ML SVO on STO (SVO/STO), and the electrochemically etched S2 with $t_{\rm final}$ (= 3 ML) and S3 with $t_{\rm final}$ (= 10 ML), taken using the atomic force microscope (AFM). The root mean square (RMS) roughnesses of LSAT and STO are 0.19 and 0.09 nm, respectively. The RMS roughnesses of SVO/LSAT and SVO/STO are 0.10 and 0.13 nm, respectively, indicating that the as-deposited SVO films have flat surfaces, with roughness less than the lattice constant.

We performed electrochemical etching with an EDLT configuration, as schematically drawn in the inset of Fig. 2(b). The upper panel of Fig. 2(a) shows the temporal change in the gate bias ($V_{\rm G}$) and gate current ($I_{\rm G}$) during etching. When applying a negative $V_{\rm G}$, $I_{\rm G}$ flowed from the SVO channel to the gate electrode, and anions with equal charges flowed from the gate electrode to the SVO channel through the IL, resulting in an electrochemical etching reaction at the interface between the IL and SVO channel. The reacted amount of the SVO channel is proportional to the absolute value of the Faradaic charge (Q_F), where Q_F is a temporal integration of $I_{\rm G}$; $Q_F = \int I_G dt$. Therefore, Q_F is proportional to a change in the thickness (Δt): $\Delta Q_F \propto \Delta t$. Thus, as shown in the lower panel of Fig. 2(a), the sheet conductance of the channel ($1/R_s$) decreased proportionally to Δt and $\Delta|Q_F|$. Figure 2(b) shows $1/R_s$ as a function of $\Delta|Q_F|$ during etching processes for three samples (S1–S3). After —five to seven cycles of etching $1/R_s$ decreased to zero. The "final thickness" is the thickness of the film just before the final process. The film thicknesses after each cycle were estimated from the initial thicknesses, final thicknesses, and the relationship $\Delta Q_F \propto \Delta t$. We determined the final thickness based on the transport data obtained for each etched film [30]. As shown in Fig. 2(b), the final thickness of S3 is estimated to be nearly 4 nm, assuming that the simple linear relation holds in the entire thickness: $\frac{t_{\rm etch}}{13\ {\rm nm}} = \frac{1/R_s(t_{\rm etch})}{1/R_s(13\ {\rm nm})}$, which is almost equal to that (5 nm) estimated by the TEM image, as shown in Fig. SI–4 [30]. A detailed method is described in the Supplemental Material, Sec. A [30].

The uniformity and film thickness after electrochemical etching were estimated with AFM and TEM as shown in Fig. 1(d) and the Supplemental Material, Sec. B [30], respectively. As shown in Fig. 1(d), the RMS roughnesses of the electrochemically etched S2 and S3 are 0.82, and 0.73 nm, respectively, which correspond to two lattice constant values. The results indicate that the uncertainty in etched S2 with $t_{\rm final} = 3$ ML ML is nearly 2 ML.

B. Transport properties

We examined the temperature dependence of ρ for the etched SVO/LSAT films and as-deposited SVO/STO films with various thicknesses. All SVO films except for the as-deposited film with thickness ($t_{\rm depo}$) = 7 ML showed an increase in ρ near 300 K with decreasing film thickness. All of the etched films showed metallic behavior with resistivity minima at $T_{\rm min}$, as shown in Figs. 3(b) and 3(c). The $T_{\rm min}$ for the etched films shifted to higher temperatures with reduced film thickness. In contrast, Fig. 3(a) shows that the as-deposited films with $t_{\rm depo} = 7$ and 6 ML exhibited insulating behavior over the entire temperature range. For the 7 ML thick film, we did not measure the resistivity between 100 and 165 K, because it took a long time for the signal to

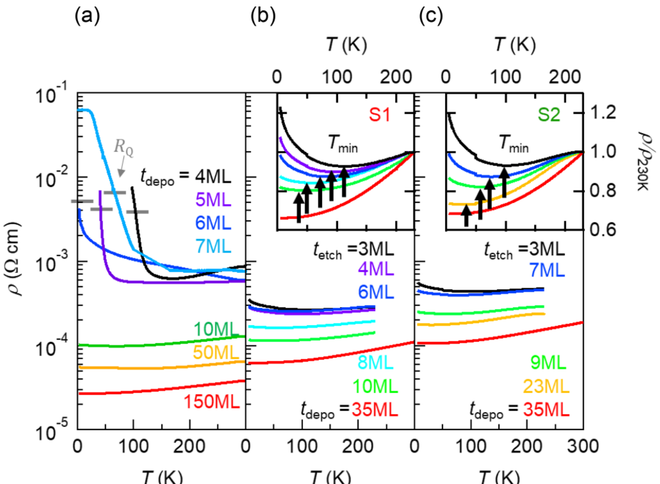

FIG. 3. (a) Temperature dependence of the resistivity (ρ) for the as-deposited SVO/STO films with thicknesses (t_{depo}) ranging from 4 to 150 monolayers (ML). The gray lines correspond to ρ, where R_s is equal to the quantum resistance $R_Q = h/e^2 \sim 25$ kΩ. (b), (c) Temperature dependence of ρ for the etched samples (b) S1 and (c) S2 with thicknesses (t_{etch}) ranging from 3 to 35 ML. The insets show ρ normalized to that at 230 K ($\rho/\rho_{230\,K}$) as a function of temperature. Black arrows show the temperatures for the resistivity minima (T_{min}).

stabilize. This is often the case with large resistance samples with large contact resistance. A small peak structure of R_s which is visible at around 280 K is probably an artifact of the measurement, resulting from the large contact resistance. The as-deposited films with $t_{depo} = 5$ and 4 ML showed metallic behavior above 50 and 120 K, respectively, and showed a rapid increase in ρ at lower temperatures. In the metallic regime, the temperature dependence of ρ can be expressed by $\rho = \rho_0 + AT^2$, corresponding to a Fermi liquid system, as shown in Fig. 4(a) by red dotted lines. The etched films also follow this relation in the metallic regime (a detailed discussion is given in Fig. 7).

Let us first focus on the temperature dependence of R_s for the as-deposited SVO/STO films with t_{depo} ranging from 4 to 7 ML. The as-deposited films with $t_{depo} = 4$, 5, and 7 ML showed a crossing of the sheet resistance (R_s) with the quantum resistance $R_Q = \frac{h}{e^2} \sim 25\text{k}\Omega$. In 2D, R_s is related to $k_F l$ by

$$k_F l = \frac{R_Q}{R_S}, \tag{1}$$

where l is the mean free path and k_F is the Fermi wave vector. A system with R_s above h/e^2 has $k_F l < 1$ and shows insulating behavior [15,31]. A previous study for semiconductors reported metallic and insulating behavior for samples with R_s below and above h/e^2, respectively, over the entire temperature range [32]. This differs from our observation for the as-deposited SVO films. The crossing of R_s with h/e^2 has also been reported in other strongly correlated systems [15,18,22]. This suggests that the insulating behavior in the ultrathin as-deposited SVO films is induced not only by a reduction in the film thickness itself but also by disorder in the films. This insulating behavior is described by the 2D Mott variable range hopping (2D VRH) model. In this model, $1/R_s$ is expressed as follows:

$$\frac{R_s^{-1}}{R_Q^{-1}} = C\exp\left[-\left(\frac{T_0}{T}\right)^{\frac{1}{3}}\right], \tag{2}$$

$$T_0 = \frac{13.8}{k_B N(E_F)\xi^2}, \tag{3}$$

where k_B is the Boltzmann constant, $N(E_F)$ is the density of localized states at the Fermi level (E_F), and ξ is the localization length. As shown in Fig. 4(b), $1/R_s$ is fitted by Eq. (2) near R_Q, where the values of T_0 are extracted from the slope

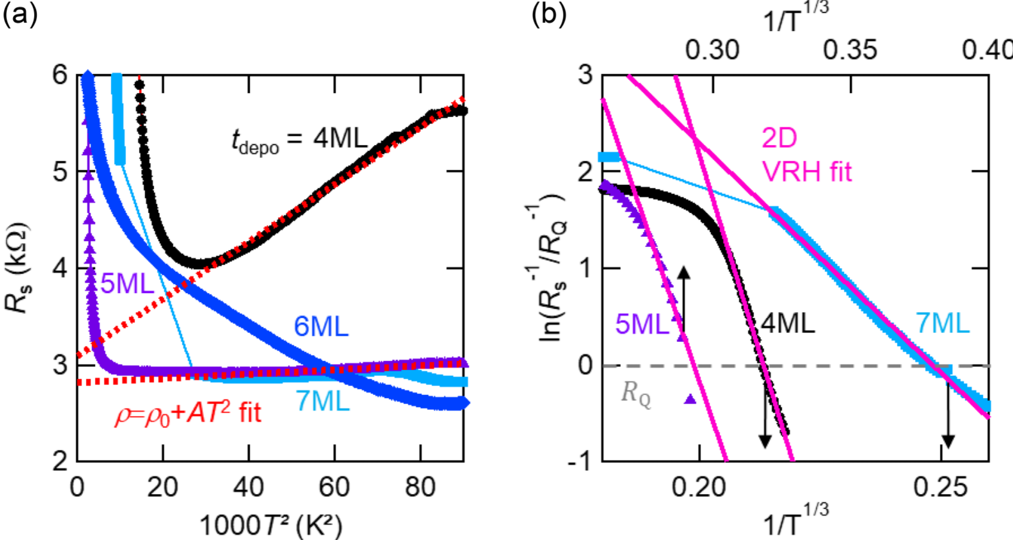

FIG. 4. (a) Sheet resistance (R_s) as a function of T^2 for as-deposited SVO films with t_{depo} ranging from 4 to 7 ML. Fits to $\rho = \rho_0 + AT^2$ are also shown as red dotted lines. (b) $\ln(R_s^{-1}/R_Q^{-1})$ as a function of $1/T^{1/3}$ for the as-deposited films with t_{depo} ranging from 4 to 7 ML. Magenta straight lines correspond to fits of the data to the 2D variable range hopping (VRH) model. The gray dotted line marks the location of zero, where R_s is equal to R_Q.

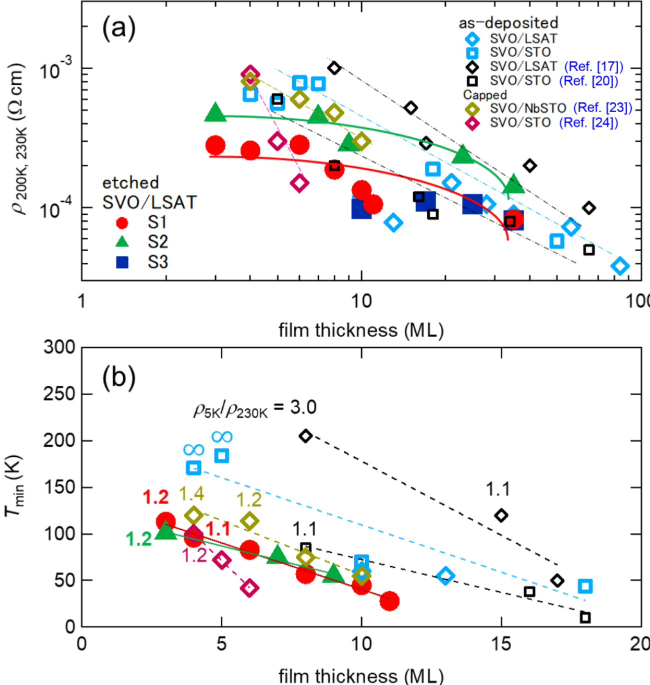

FIG. 5. (a) ρ at 200 K ($\rho_{200\,\mathrm{K}}$) plotted against the film thickness on a log-log scale for S1 (red solid circles) and S2 (green solid triangles). For S3, ρ at 230 K ($\rho_{230\,\mathrm{K}}$) is plotted with blue solid squares. Data for the as-deposited films (SVO/LSAT and SVO/STO) and those (SVO/LSAT [17], SVO/STO [20], capped SVO/NbSTO [23], and capped SVO/STO [24]) obtained from the literature are plotted. All lines are guides to the eye. (b) $T_{\min}$ as a function of the film thickness on a linear scale for S1 and S2 and as-deposited films. The symbols are the same as in (a). The values of $\rho_{5\,\mathrm{K}}/\rho_{230\,\mathrm{K}}$ are also shown for the films with $\rho_{5\,\mathrm{K}}/\rho_{230\,\mathrm{K}} > 1$. We denote $\rho_{5\,\mathrm{K}}/\rho_{230\,\mathrm{K}}$ as ∞ when ρ exhibits an abrupt increase by more than one order of magnitude above 50 K upon cooling. All lines are guides to the eye.

to be 1.08×10^5, 5.86×10^5, and 4.42×10^6 K for the films with $t_{\mathrm{depo}} = 7$, 5, and 4 ML, respectively. According to VRH theory [22,33,34], the mean hopping distance (l_{hop}) is given by $l_{\mathrm{hop}} = (\frac{T_0}{T})^{\frac{1}{3}}\xi/3$, where l_{hop} must be larger than ξ, namely, $l_{\mathrm{hop}}/\xi > 1$. We estimated the value of l_{hop}/ξ at characteristic temperatures T_Q, where $R_s(T_Q) = R_{\mathrm{Q}}$, to be 3.94, 8.09, and 11.7 for the films with $t_{\mathrm{depo}} = 7$, 5, and 4 ML, respectively. All these values are larger than 1, which is consistent with VRH theory. By reducing t_{depo} from 7 to 4 ML, T_0 is increased by more than one order of magnitude and, thus, $N(E_{\mathrm{F}})\xi^2$ is decreased by the same order of magnitude according to Eq. (3). It is unlikely that N (E_{F}) decreases by more than one order of magnitude by reducing t_{depo} from 7 to 4 ML. Therefore, ξ would be decreased by a factor of 6 or 7 by reducing t_{depo}; in other words, localization effects are enhanced by reducing the film thickness for the as-deposited ultrathin films.

Next, we examined the thickness dependence of the transport data for the etched and as-deposited films. Figure 5(a) shows plots of ρ at 200 K ($\equiv \rho_{200\,\mathrm{K}}$) against the film thickness on a double logarithmic scale. Red solid circles and green solid triangles represent the data for the etched films S1 and S2, respectively. For S3, only the available data at 230 K ($\rho_{230\,\mathrm{K}}$) are plotted with blue solid squares. Data for the as-deposited films (SVO/LSAT and SVO/STO) and those obtained from the literature are also plotted [17,20,23,24]. Figure 5(b) displays $T_{\min}$ versus the film thickness for the etched S1 and S2 films and as-deposited films on a linear-linear scale, where the symbols are the same as in (a). For all the films except for S3, we found a trend in which $\rho_{200\,\mathrm{K}}$ increased by one order of magnitude with decreasing film thickness from 50 to 10 ML to 6 ML. $T_{\min}$ also showed a significant increase with decreasing film thickness, indicating the occurrence of insulating behavior at higher temperatures.

We interpret these results in terms of a metal to Mott insulator transition being associated with the reduction of the film thickness (reduced dimensionality). According to the Hubbard model, a system shows a transition from metallic to Mott insulator states with decreasing bandwidth (W), and it is known that W in a 2D system is smaller than that in a 3D system. In this framework, therefore, the observed increase in $\rho_{200\,\mathrm{K}}$ and $T_{\min}$ with decreasing film thickness is attributed to the change in the electronic states from metallic to Mott insulator states due to the reduced W.

For both the as-deposited and etched films shown in Fig. 5(a), we observed a common trend for $\rho_{200\,\mathrm{K}}$, which increased with decreasing film thickness. On the other hand, the value of $\rho_{200\,\mathrm{K}}$ for a given thickness differs largely (which spans a factor of 3–5), depending on the series of SVO films. The difference in $\rho_{200\,\mathrm{K}}$ for a given thickness observed among the series of SVO films can result from the difference in disorder in the films such as oxygen vacancy, defects, and surface degradations in the as-deposited samples. Although the as-deposited samples were fabricated with the same deposition temperature and pressure, the laser energy and the target condition in our experiment were inevitably changed between depositions. In particular, for the series of as-deposited films, it is even difficult to draw individual smooth lines of a similar shape on which data points fall. For the S1 and S2 etched films, all the data points in each series fall on nearly smooth lines of similar shape, suggesting that the disorder is not significantly changed during etching. Notably, for the S1 and S2 etched films, the saturation of $\rho_{200\,\mathrm{K}}$ is observed below 6 and 7 ML, respectively. This saturation corresponds to the unexpected increase of carrier density during the electrochemical etching (a discussion is given in Fig. 6).

The data points for $T_{\min}$ versus thickness for S1 and S2 fall on a single line, in contrast to the behavior observed for the as-deposited films. Furthermore, the $T_{\min}$ versus thickness line for the etched S1 and S2 films indicated with full lines is located below the $T_{\min}$ versus thickness line for as-deposited films [17,20], while $T_{\min}$'s for our etched films are comparable to those for the capped films [23,24]. These features strongly suggest that the etched films have small disorder, which is introduced before etching, and its strength stays nearly constant even after the films are etched down to 3 ML. The small disorder in the S1 and S2 etched films explains the weakly insulating behavior observed at low temperature down to the ultrathin regime, as shown in Figs. 3(b) and 3(c).

To heuristically quantify the strength of the localization effects at low temperature in each film, we focus on the ratio of ρ at the lowest temperature to that at high temperature, $\rho_{5\,\mathrm{K}}/\rho_{230\,\mathrm{K}}$. Then, we defined the films with $\rho_{5\,\mathrm{K}}/\rho_{230\,\mathrm{K}} > 1$ as "insulating" and the other films as "weakly insulating."

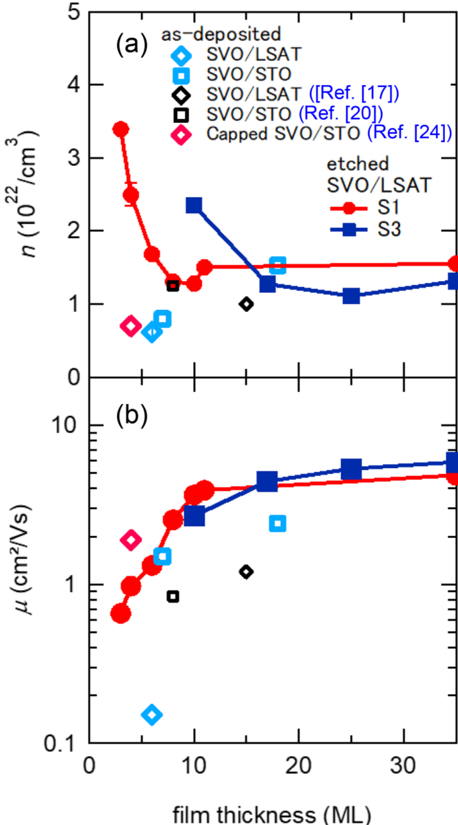

FIG. 6. (a) Carrier density (n) and (b) mobility (μ) as a function of the film thickness at 200 K for S1 (red solid circles) and at 230 K for S3 (blue solid squares). Data for the as-deposited films (SVO/LSAT at 300 K and SVO/STO at 100 K) and those (SVO/LSAT [17], SVO/STO [20], and capped SVO/STO [24] at 200 K) obtained from the literature are also plotted.

In Fig. 5(b), we show the values of $\rho_{5\,\mathrm{K}}/\rho_{230\,\mathrm{K}}$ for the insulating films with $\rho_{5\,\mathrm{K}}/\rho_{230\,\mathrm{K}} > 1$. Upon cooling, ρ for the as-deposited films with $t_{\mathrm{depo}} < 7$ ML showed an abrupt increase by more than one order of magnitude above 50 K. Hence, we denote $\rho_{5\,\mathrm{K}}/\rho_{230\,\mathrm{K}}$ as ∞. It is notable that even for the 15 ML thick film, the as-deposited film is insulating [17]. Similar insulating behaviors with thicknesses of approximately 10 ML have been reported in transition metal oxide thin films, such as $CaVO_3$ [16], $NdNiO_3$ [21], and $LaNiO_3$ [14]. In addition, an abrupt increase in ρ, corresponding to a $\rho_{5\,\mathrm{K}}/\rho_{230\,\mathrm{K}}$ value of ∞, at low temperature has also been reported for ultrathin films of $La_{2/3}Sr_{1/3}MnO_3$ [19] and $SrRuO_3$ [18]. These insulating behaviors have been considered to be due to various disorder effects in thin films, such as strain effects due to the substrate, oxygen vacancies, and surface effects [19,21].

For the S1 and S2 films, the etched films with thicknesses above 6 ML were "weakly insulating", and only the 3 and 4 ML thick films were insulating. Moreover, the value of $\rho_{5\,\mathrm{K}}/\rho_{230\,\mathrm{K}}$ for the thinnest (3 ML) films is at most 1.2. These results indicate that the etched films are robust against disorder. A previous study using *in situ* photoemission (PES) showed that Mott insulating states are induced in ultrathin SVO films with a thickness lower than 3 ML [25]. Thus, we conclude that the SVO ultrathin films fabricated by electrochemical etching have very low disorder effects comparable to an *in situ* SVO film. The etching process was carried out in He gas, and any absorbed atoms on the film were removed during the etching. The surface of the film was coated by specific adsorption of hydrophobic anions during electrochemical etching, and then the surface condition was unchanged during the etching. The most current studies of SVO also elucidated that high-quality capped film exhibited a weakly insulating behavior down to 5–6 ML without an abrupt increase of ρ [23,24]. Therefore, the insulating behavior of the as-deposited SVO films is most likely induced by surface conditions under ambient conditions.

The carrier density (n) and electron mobility (μ) were estimated from Hall measurements for the etched films and as-deposited films. As shown in Fig. 6(a), for all the films, n was almost independent of the film thickness above 10 ML, suggesting that thicker films above 10 ML are bulklike. The S1 and S3 etched films showed an increase in n with decreasing film thickness below approximately 10 ML, as shown with red solid circles and blue solid squares, respectively, contrasting with a decrease in n for the as-deposited films shown with open symbols. The decrease in n observed for the as-deposited films most likely originates from increased disorder for the thinner films, such as surface effects and defects at the interface between the film and the substrate. The increase in n observed for the etched films might originate from unexpected intercalation of ions into the film or adsorption of ions on the film during the electrochemical etching process.

As shown in Fig. 6(b), the data points for μ for the S1 and S3 etched films fall on nearly the same smooth curve that shows a decrease with reducing film thickness below approximately 10 ML. The as-deposited films also showed a decreasing trend for μ with decreasing film thickness; however, μ for the as-deposited films with the same thicknesses differed from each other. This indicates that each as-deposited film had different disorder effects. The monotonic decrease in μ with decreasing film thickness can result from two origins: first, an increase in disorder around the interface between the film and the substrate, and, secondly, from an enhancement of the electron effective mass, which is expected for a system approaching the MIT with decreasing dimensionality.

According to the Fermi liquid theory, the temperature dependence of ρ in a Fermi liquid system is expressed by $\rho = \rho_0 + AT^2$, where the residual resistivity ρ_0 is attributed to static disorder [35,36] and the parameter A is related to an electron effective mass enhanced by an electron-electron interaction in a strongly correlated metal [10]. In our experiment, ρ-T curves with various thicknesses follow that relationship at high temperatures above T_{min}. Typical results for the fitting are shown for S1 films with $t_{\mathrm{etch}} = 6$ and 10 ML by dashed lines in Fig. 7(a), together with the $\rho - \rho_0$ versus T data indicated by blue and green lines, respectively.

Figures 7(b) and 7(c) display the parameters ρ_0 and A, respectively, extracted from the fitting as a function of the film thickness for S1 (red solid circles), S2 (green solid triangles), and S3 (blue solid squares). Open symbols in Figs. 7(b) and 7(c) denote the parameters ρ_0 and A, respectively, for the as-deposited films (SVO/LSAT and SVO/STO), where black diamonds and squares denote data obtained from

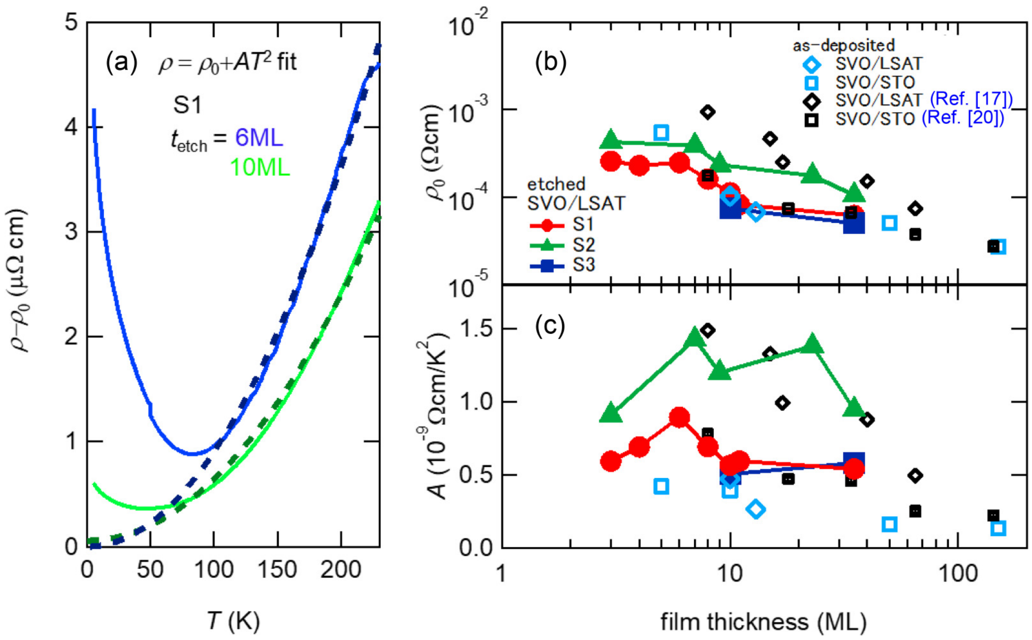

FIG. 7. (a) ρ-ρ_0 as a function of T for S1 with $t_{\rm etch} = 6$ ML (blue) and 10 ML (green). Dashed lines represent the $\rho = \rho_0 + AT^2$ fits. (b) The fitted parameters ρ_0 and (c) A for S1 (red solid circles), S2 (green solid triangles), and S3 (blue solid squares) plotted against the film thickness. Open symbols represent the data for the as-deposited films (SVO/LSAT and SVO/STO), where black diamonds and squares denote data obtained from Refs. [17,20], respectively.

Refs. [17,20], respectively. Figure 7(b) shows that for all the films, the dependence of ρ_0 on the film thickness is nearly the same as that of $\rho_{200\,\rm K}$ (or $\rho_{230\,\rm K}$) on the film thickness, indicating that ρ_0 and $\rho_{200\,\rm K}$ (or $\rho_{230\,\rm K}$) reflect essentially the same properties related to static disorder. Figure 7(c) shows that for both etched and as-deposited films, A shows a roughly increasing trend with decreasing film thickness from approximately 30 to 100 ML down to 6–7 ML. For S1 and S2, in particular, as $t_{\rm etch}$ is reduced below approximately 10 ML, after showing a small peak at approximately 6–7 ML, A exhibits a decrease in the thinnest region of 3–6 ML.

According to Ref. [37,38], A is expressed by the following equation:

$$A = \left(\frac{4\pi^2 k_{\rm B}^2}{e^2\hbar^2}\right)\left(\frac{m_b}{n}\right)\Phi, \tag{4}$$

where $k_{\rm B}$ is the Boltzmann constant, e is the elementary charge, $\hbar$ is the Planck constant divided by 2π, m_b is the band mass, and Φ is the coefficient of the scattering rate. An enhancement of electron-electron interactions leads to an increase in $m_b\Phi$, which, in turn, results in an increase in A, in accordance with Eq. (4). Equation (4) also indicates that an increase in n leads to a reduction in A. Indeed, a decrease in A associated with an increase in n has been reported for $SrTi_{1-x}V_xO_3$ near the MIT [39,40].

The increase in A observed below 10 ML down to 6–7 ML for the etched films is attributed to an enhanced $m_b\Phi$ due to enhanced electron-correlation effects induced by the reduced film thickness. In contrast, the decrease in A observed below 6–7 ML cannot be explained by the enhanced electron-correlation effects mentioned above. We consider that this is due to the competing effects between a pronounced increase in n shown in Fig. 6(a) and a moderate increase in $m_b\Phi$ due to the enhanced electron correlation. The former effect is more dominant than the latter.

C. Low temperature resistivity and magnetoresistance

All of the etched SVO films exhibit a metallic behavior with a resistivity upturn at low temperature. We examine the origin of the resistivity upturn in the etched films. Near the metal-insulator transition, electrons are weakly localized, and the conductivity is affected by electron-electron interactions and interference. In this regime, the resistivity upturn has been previously interpreted using the concept of quantum corrections $\Delta\sigma(T)$ to the conductivity $\sigma(T)$ (QCC) [41,42]. The QCC is explained by two contributions: weak localization (WL) and a renormalized electron-electron interaction (REEI). We define $\Delta\sigma(T)$ as a correction to the Fermi liquid model. Then, ρ is expressed as follows:

$$\rho = \frac{1}{\sigma_0 + \Delta\sigma(T)} + AT^2, \tag{5}$$

where σ_0 is the residual conductivity and A is the parameter in the Fermi liquid model mentioned above. The WL is reflected in a resistivity correction due to electron interference scattering by defects or impurities [41,42], and the REEI originates from the density of state correction at the Fermi level.

In the 3D and 2D QCC models, $\Delta\sigma$ is expressed as follows:

$$\Delta\sigma_{\rm 3D} = a_1 T^{\frac{q}{2}} + a_2 T^{\frac{1}{2}}, \tag{6}$$

$$\Delta\sigma_{\rm 2D} = a\ln T = \frac{e^2}{\pi h}(p+F)\ln T, \tag{7}$$

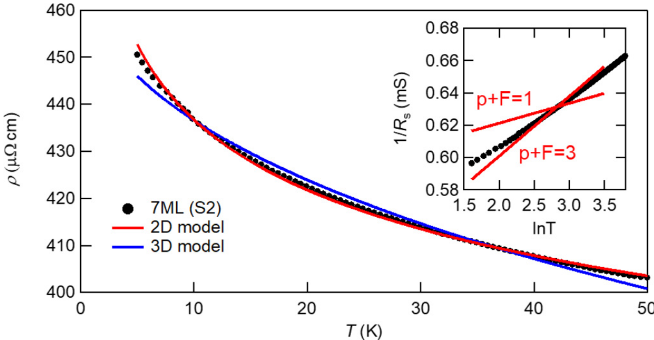

FIG. 8. ρ-T data for the 7 ML thick S2 film. Blue and red lines represent fits of the data to Eq. (6) (3D QCC model) and Eq. (7) (2D QCC model), respectively. The inset shows $1/R_s$ versus the logarithm of temperature for the same data. Two straight red lines with small and large slopes correspond to the fits to Eq. (7) with $p + F = 1$ and 3, respectively.

where a_1, q, and p arise from WL, and a_2 and F correspond to the contribution from REEI. When electron-electron scattering governs the conductivity, the parameters q and p are equal to 2 and 1, respectively, while q and p are both equal to 3 for electron-phonon scattering. In addition, the correction due to the WL is always positive, so the parameters a_1 and p are positive.

We fitted the ρ-T data for various thicknesses using Eqs. (6) and (7) with a fixed $q = 3$. Figure 8 shows typical results for the fitting of ρ (T) for the 7 ML thick S2 film. The 2D fit (red line) follows the experimental data better than the 3D fit (blue line). This indicates that the 2D QCC model is better applied to describe ρ (T) for the etched films. The parameter $p + F$ in Eq. (7) can be extracted from the slope of $1/R_s$ versus the logarithm of temperature, as shown in the inset of Fig. 8. The p+F values for the S1 films with $t_{\mathrm{etch}} = 10, 8, 6, 4$, and 3 ML are 2.8, 2.7, 3.0, 3.0, and 2.8, respectively. For the S2 films with $t_{\mathrm{etch}} = 9, 7$, and 3 ML, the p+F values are 2.8, 2.4, and 1.5, respectively. Thus, all these p+F values turn out to range between 1 and 3. Although we are unable to specify each value of p and F separately, considering the theoretical prediction that p is either 1 or 3, the present result strongly suggests that F is at most of the order of 0.1, i.e., the contribution of WL is more important than that of REEI. Indeed, it has been reported that F ranges from 0.34 to 0.57 in Ref. [43]. As mentioned above, for all the etched films except for the 3 ML thick S2 film, the values of p+F remain at approximately 3. This finding indicates that electron-phonon scattering is the dominant scattering mechanism rather than electron-electron scattering.

We measured ρ for S2 films with different film thicknesses as a function of the perpendicular magnetic field (B) at 5 K. Figure 9(a) shows the normalized magnetoresistance (MR), which is defined as $100 \times [\rho(B) - \rho(0)]/\rho(0)$. All S2 films with thicknesses ranging from 3 to 23 ML showed a positive MR. For some semiconductors, a positive MR with a parabolic shape, MR $\approx (\mu B)^2$, was reported, whose origin is attributed to a Lorenz force. However, in our case, $(\mu B)^2$ is estimated to be as small as 10^{-5}% for 3 T, which is three orders of magnitude smaller than the observed value.

We show, instead, that our positive MR is well explained in terms of the weak antilocalization (WAL) effect for a weakly disordered metal [20,44–46]. The magnetoconduc-

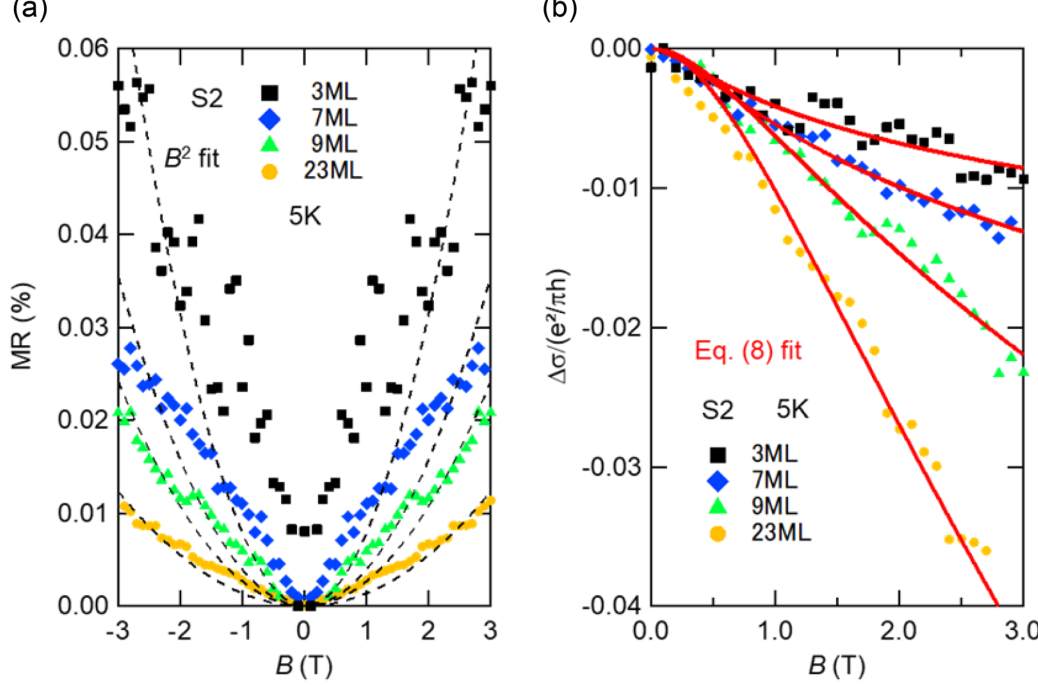

FIG. 9. (a) Perpendicular magnetic field (B) dependence of the normalized magnetoresistance (MR), $100 \times [\rho(B) - \rho(0)]/\rho(0)$, for S2 with thicknesses ranging from 3 to 23 ML at 5 K, where $\rho(0)$ is the resistivity minimum in the MR curve. Dashed lines are B^2 fits. (b) Magnetoconductance normalized by the quantum conductance $(e^2/\pi h)$ as a function of B for samples with thicknesses ranging from 3 to 23 ML. Red lines are fits to the data based on Eq. (8).

tance is well described by the Hikami-Larkin-Nagaoka (HLN) equation in 2D, where the spin-orbit length, l_{so}, is negligibly smaller than the inelastic scattering length, l_{in} ($l_{so} \ll l_{in}$) [44]:

$$[\sigma(B) - \sigma(0)] \Big/ \left(\frac{e^2}{\pi h}\right) = \alpha \left[\ln\left(\frac{B_{in}}{B}\right) - \psi\left(\frac{1}{2} + \frac{B_{in}}{B}\right) \right], \quad (8)$$

$$B_{in} = \frac{h}{8\pi l_{in}^2}, \quad (9)$$

where ψ is the digamma function, B_{in} is a characteristic magnetic field for inelastic scattering, and l_{in} is the inelastic mean free path. Figure 9(b) shows the magnetoconductance converted from the MR data in Fig. 9(a) and fits to the data based on the HLN equation [Eq. (8)]. The fitting parameter α is an indication of the dominant effect: $\alpha = -1$ for WL and $0 < \alpha < 1/2$ for WAL. For films with thickness of 23 ML (∼ 8.8 nm), 9 ML, 7 ML, and 3 ML, α is determined to be 0.098, 0.034, 0.011, and 0.0053, and l_{in} is determined to be 17, 21, 32, and 41 nm, respectively. l_{in} is always larger than the film thickness, and, thus, it is confirmed that the etched films are in the 2D regime.

Interestingly, competition between WAL and WL effects has been reported in the weakly localized regime above 5 K for as-deposited SVO films with thicknesses of 4 and 5 ML [23]. This indicates that l_{so} is of the same order of magnitude as l_{in} for the films in Ref. [23]. It is considered that l_{so} for our etched SVO films is almost the same as that for the as-deposited SVO films in Ref. [23] because l_{so} is determined by the spread of the *d* orbital of vanadium; namely, it only depends on the compound. Therefore, l_{in} for our films is larger than in Ref. [23], indicating that the disorder effects for our etched films are smaller than those for the as-deposited films in Ref. [23].

IV. CONCLUSION

We fabricated conductive ultrathin SVO films by electrochemical etching, which exhibited metallic behavior down to 3 ML. The films showed a systematic change in transport properties with decreasing film thickness, indicating that the disorder remained nearly unchanged during etching and that only the thickness was reduced. In contrast, the as-deposited ultrathin SVO films behaved like a strongly localized metal, which was attributed to disorder introduced during deposition. The resistivity $\rho(T)$ was observed to show insulating behavior for the as-deposited ultrathin films below 10 ML, which was reproduced by a 2D VRH model, in which the localization length decreased with decreasing film thickness.

For the etched films, the electron mobility measured at 200 K showed a decrease with decreasing film thickness below 10 ML. This was interpreted as originating from an increased scattering rate and an enhanced electron effective mass, as expected for a system approaching a MIT with reduced dimensionality. The etched films and most of the as-deposited films showed Fermi liquid behavior in the high-temperature regime. In the low-temperature regime, a slight upturn in $\rho(T)$ and a positive MR were observed for the etched films down to 3 ML, which was explained in terms of weak antilocalization theory for a weakly disordered metal.

ACKNOWLEDGMENTS

This work was supported in part by JSPS KAKENHI (Grants No. 21H01038 and No.19H02798) and CREST-JST (Grant No. JPMJCR15Q2).

[1] N. F. Mott, Proc. Phys. Soc., London, Sect. A **62**, 416 (1949).
[2] N. F. Mott, *Metal-Insulator Transitions*, 2nd ed. (Taylor and Francis, London, 1990).
[3] P. W. Anderson, Phys. Rev. **109**, 1492 (1958).
[4] M. Imada, A. Fujimori, and Y. Tokura, Rev. Mod. Phys. **70**, 1039 (1998).
[5] F. Inaba, T. Arima, T. Ishikawa, T. Katsufuji, and Y. Tokura, Phys. Rev. B **52**, 2221(R) (1995).
[6] S. Miyasaka, T. Okuda, and Y. Tokura, Phys. Rev. Lett. **85**, 5388 (2000).
[7] T. M. Dao, P. S. Mondal, Y. Takamura, E. Arenholz, and J. Lee, Appl. Phys. Lett. **99**, 112111 (2011).
[8] I. H. Inoue, I. Hase, Y. Aiura, A. Fujimori, Y. Haruyama, T. Maruyama, and Y. Nishihara, Phys. Rev. Lett. **74**, 2539 (1995).
[9] M. J. Rozenberg, I. H. Inoue, H. Makino, F. Iga, and Y. Nishihara, Phys. Rev. Lett. **76**, 4781 (1996).
[10] I. H. Inoue, O. Goto, H. Makino, N. E. Hussey, and M. Ishikawa, Phys. Rev. B **58**, 4372 (1998).
[11] M. Takayanagi, T. Tsuchiya, W. Namiki, S. Ueda, M. Minohara, K. Horiba, H. Kumigashira, K. Terabe, and T. Higuchi, Appl. Phys. Lett. **112**, 133106 (2018).
[12] H. Y. Wang, Y. Iwasa, M. Kawasaki, B. Keimer, N. Nagaosa, and Y. Tokura, Nat. Mater. **11**, 103 (2012).
[13] R. Ramesh and D. G. Schlom, Nat. Rev. Mater. **4**, 257 (2019).
[14] J. Son, P. Moetakef, J. M. LeBeau, D. Ouellette, L. Balents, S. J. Allen, and S. Stemmer, Appl. Phys. Lett. **96**, 062114 (2010).
[15] R. Scherwitzl, S. Gariglio, M. Gabay, P. Zubko, M. Gilbert, and J. M. Triscone, Phys. Rev. Lett. **106**, 246403 (2011).
[16] M. Gu, J. Laverock, B. Chen, K. E. Smith, S. A. Wolf, and J. Lu, J. Appl. Phys. **113**, 133704 (2013).
[17] M. Gu, S. A. Wolf, and J. Lu, Adv. Mater. Interfaces **1**, 1300126 (2014).
[18] X. Shen, X. Qiu, D. Su, S. Zhou, A. Li, and D. Wu, J. Appl. Phys. **117**, 015307 (2015).
[19] Z. Liao, F. Li, P. Gao, L. Li, J. Guo, X. Pan, R. Jin, E. W. Plummer, and J. Zhang, Phys. Rev. B **92**, 125123 (2015).
[20] A. Fouchet, M. Allain, B. Berini, E. Popova, P. E. Janolin, N. Guiblin, E. Chikoidze, J. Scola, D. Hrabovsky, Y. Dumont, and N. Keller, Mater. Sci. Eng. B **212**, 7 (2016).
[21] L. Wang, S. Ju, L. You, Y. Qi, Y. W. Guo, P. Ren, Y. Zhou, and J. Wang, Sci. Rep. **5**. 18707 (2016).

[22] L. Wang, L. Chang, X. Yin, A. Rusydi, L. You, Y. Zhou, L. Fang, and J. Wang, J. Phys.: Condens. Matter **29**, 025002 (2017).
[23] G. Wang, Z. Wang, M. Meng, M. Saghayezhian, L. Chen, C. Chen, H. Guo, Y. Zhu, E. W. Plummer, and J. Zhang, Phys. Rev. B **100**, 155114 (2019).
[24] J. Wang, N. Gauquelin, M. Huijben, J. Verbeeck, G. Rijnders, and G. Koster, Appl. Phys. Lett. **117**, 133105 (2020).
[25] K. Yoshimatsu, T. Okabe, H. Kumigashira, S. Okamoto, S. Aizaki, A. Fujimori, and M. Oshima, Phys. Rev. Lett. **104**, 147601 (2010).
[26] J. Shiogai, Y. Ito, T. Mitsuhashi, T. Nojima, and A. Tsukazaki, Nat. Phys. **12**, 42 (2016).
[27] M. Yoshida, J. Ye, T. Nishizaki, N. Kobayashi, and Y. Iwasa, Appl. Phys. Lett. **108**, 202602 (2016).
[28] S. Kouno, Y. Sato, Y. Katayama, A. Ichinose, D. Asami, F. Nabeshima, Y. Imai, A. Maeda, and K. Ueno, Sci. Rep. **8**, 14731 (2018).
[29] N. Shikama, Y. Sakishita, F. Nabeshima, Y. Katayama, K. Ueno, and A. Maeda, Appl. Phys. Express **13**, 083006 (2020).
[30] See Supplemental Material at http://link.aps.org/supplemental/10.1103/PhysRevB.105.045138 for the thickness estimations of the etched films.
[31] D. C. Licciardello and D. J. Thouless, Phys. Rev. Lett. **35**, 1475 (1975).
[32] M. Nakano, A. Tsukazaki, A. Ohtomo, K. Ueno, S. Akasaka, H. Yuji, K. Nakahara, T. Fukumura, and M. Kawasaki, Adv. Mater. **22**, 876 (2010).
[33] N. F. Mott and E. A. Davis, *Electronic Processes in Non-Crystalline Materials, Oxford Classic Texts in the Physical Sciences* (Clarendon Press, Oxford, 1970).
[34] Z. H. Khan, M. Husain, T. P. Perng, N. Salah, and S. Habib, J. Phys.: Condens. Matter **20**, 475207 (2008).
[35] I. H. Inoue, H. Makino, I. Hase, M. Ishikawa, N. E. Hussey, and M. J. Rozenberg, Phys. B (Amsterdam, Neth.) **237**, 61 (1997).
[36] Y. C. Lan, X. L. Chen, and M. He, J. Alloys Compd. **354**, 95 (2003).
[37] N. E. Hussey, J. Phys. Soc. Jpn. **74**, 1107 (2005).
[38] D. Oka, Y. Hirose, S. Nakano, T. Fukumura, and T. Hasegawa, Phys. Rev. B **92**, 205102 (2015).
[39] K. Hong, S. H. Kim, Y. J. Heo, and Y. U. Kwon, Solid State Commun. **123**, 305 (2002).
[40] M. Gu, S. A. Wolf, and J. Lu, Appl. Phys. Lett. **103**, 223110 (2013).
[41] G. Bergmann, Phys. Rep. **107**, 1 (1984).
[42] P. A. Lee and T. V. Ramakrishnan, Rev. Mod. Phys. **57**, 287 (1985).
[43] S. Mukhopadhyay and I. Das, J. Phys.: Condens. Matter **21**, 186004 (2009).
[44] S. Hikami, A. I. Larkin, and Y. Nagaoka, Prog. Theor. Phys. **63**, 707 (1980).
[45] A. D. Caviglia, M. Gabay, S. Gariglio, N. Reyren, C. Cancellieri, and J. M. Triscone, Phys. Rev. Lett. **104**, 126803 (2010).
[46] M. Liu, J. Zhang, C. Z. Chang, Z. Zhang, X. Feng, K. Li, K. He, L. I. Wang, X. Chen, X. Dai, Z. Fang, Q. K. Xue, X. Ma, and Y. Wang, Phys. Rev. Lett. **108**, 036805 (2012).